Journal of Porous Media, 18 (6): 637–652 (2015)

GEOMETRICAL CHARACTERIZATION OF KELVIN-LIKE METAL FOAMS FOR DIFFERENT STRUT SHAPES AND POROSITY

Prashant Kumar, [*] ***Frederic Topin, & Lounes Tadrist***

IUSTI, CNRS UMR 7343, Aix-Marseille Université, Marseille, France

[*]Address all correspondence to Prashant Kumar E-mail: prashant.kumar@etu.univ-amu.fr

Original Manuscript Submitted: 4/3/2014; Final Draft Received: 2/24/2015

Kelvin cell foams are an idealization of replication foams and nowadays are also materialized for various industrial purposes. There are several works dealing with thermo-hydraulic properties of foams in relation to their structure. The thermo-hydraulic behavior of open-cell foams depends on their microscopic structure. Various ideal periodic isotropic structures of tetrakaidecahedron shapes with constant cross section of the ligament having circular, square, diamond, hexagon, and star strut shapes with various orientations are studied. Computer aided design (CAD) modeling has been used to produce various shapes in the porosity range from 60 to 95%. A generalized analytical model has been proposed in order to obtain geometrical parameters correctly as they have substantial influence on thermal and hydraulic phenomena, where strut geometry is of primary importance. Various relationships between different geometrical parameters and porosities are presented. The analytical results are compared with experimental data from the literature. An excellent agreement has been observed between the predicted correlations, data obtained from CAD measurements, and experiments.

KEY WORDS: *foam geometry, characterization, metal foam, structure, strut morphology, specific surface*

1. INTRODUCTION

The properties of open-cell foams make them desirable materials for use in many applications where mechanical energy absorption and permeability characteristics are valued. They can be used in numerous industrial applications like electromagnetic radiation shielding (Losito, 2008), crash energy absorption (Jung et al., 2011), rocket jacket cooling (Avenall, 2004), heat exchangers (Kim et al., 2000), efficiency enhancement in phase change materials (Lafdi et al., 2007), etc.

Gibson and Ashby (1997) reviewed different models of cellular foam structure in which foams are considered as regular packing of various polyhedra including triangular prisms, rectangular prisms, hexagonal prisms, rhombic dodecahedra and tetrakaidecahedra. These authors preferred the tetrakaidecahedron model since it is a space filling structure and gave the most consistent agreement with observed morphological properties.

During previous decades, many researchers have assumed an idealized shape, such as Calmidi (1998) proposed the use of a cubic unit volume open-cell analytical model to approximate the metal foam structure and proposed a relationship of pore diameter as a function of porosity and "pore density" defined as pores per linear inch (PPI). Du Plessis et al. (1994) presented a model for evaluating permeability and the inertia coefficient for metal foams, which was derived by experimental results of foam samples of small pore size (45–100 PPI) and porosity (ε) of 0.973–0.978. Several researchers (Buciuman and Kraushaar-Czarnetzki, 2003; Garrido et al., 2008; Giani et al., 2005a,b; Grosse et al., 2008; Lu et al., 1998; Moreira and Coury, 2004; Stemmet et al., 2006) reported theoretical geometrical models that describe the relation between strut diameter, pore diameter, and porosity. Their proposed models are different in the relation to the porosity range studied. For the high-porosity range ($\varepsilon > 0.9$), different models exhibit equivalent results, but

1091–028X/15/$35.00

NOMENCLATURE

a_c	specific surface area, m^{-1}
a_{sw}	opening area of square face of foam structure, mm^2
a_{hw}	opening area of hexagon face of foam structure, mm^2
A/A_{side}	side length of the strut shape, mm
d_{cell}	cubic unit cell side length
d_s	strut diameter, mm
d_p	pore diameter, mm
D	sphere diameter, mm
D_c	length of cubic unit cell, mm
d_{cell}	cell diameter (cubic unit cell side length), mm
k	adjustable parameter
L_s	strut length, mm
L	node-to-node length, mm
R_{eq}	equivalent circular strut radius, mm
$S_{ligament}$	lateral surface area of one ligament, mm^2
S_{node}	lateral surface area of one node, mm^2
V_s	total solid volume of the octahedron, mm^3
$V_{ligament}$	volume of one ligament, mm^3
V_{node}	volume of one node, mm^3
V_T	volume of octahedron, mm^3
V_c	volume of cubic cell, mm^3

Greek Symbols

ε	porosity
χ	constant parameter [Eq. (9)]
ψ	constant parameter [Eq. (10)]
α_{eq}	ratio of strut diameter (or side length of strut shape) to node to node length
β	ratio of strut length to node to node length

for the low-porosity range, quite high deviations are observed. The models tend to overestimate the experimental values. In many cases, the model unit cells did not have much similarity to the synthesized structures of the open-cell foams. It is therefore evident that there are discrepancies in the geometrical values for different correlations reported in the literature. These discrepancies depend on which input parameter such as pore diameter d_p or strut diameter d_s is used to calculate the geometrical properties.

Recently, Garrido et al. (2008) evaluated pressure drop correlations from the literature by comparing the predictions with their own experimental data. It was concluded that the prediction of all of the correlations from the literature was not satisfactory. Edouard et al. (2008) reviewed state-of-the-art correlations for pressure drop prediction in foam structures. They reported that the standard deviation between experimental and theoretical values of the pressure drop can be as high as three orders of magnitude. This discrepancy may result from the combination of inaccuracy of measurements and oversimplification of the strut geometry. Moreover, the use of the same kind of hypothetical repeating unit cell as used for the description of packed beds of irregular granules or fibers cannot be applied directly to the open-cell foams as generally discussed in the literature.

A quantitative image analysis of strut shape and variation of cross sections of open-cell polyester urethane (PU) and aluminium (Al) foams having different PPI ratios were performed by Jang et al. (2008). Their analysis confirmed that the struts of both metal- and polymer-based foams present a plateau border shape. The cross-sectional area is nearly constant over the central half of the strut length, but increases rapidly when approaching the strut ends.

Depending on the manufacturing process and the type of material, foam structures exhibit different strut morphologies, namely, cylindrical, equilateral triangular, convex, and concave triangular as visualized by Bhattacharya et al. (2002) and Inayat et al. (2011). The strut cross section changes with porosity. This fact leads various authors to propose empirical correction factors to adjust the calculated values of morphological parameters. These factors, however, are sensitive to both porosity range and foam strut configuration.

Accurate evaluation of geometrical properties of foams thus becomes critical for various uses as thermophysical and flow properties depend strongly on local morphology of both pore and solid matrix (De Jaeger et al., 2011; Hugo and Topin, 2012; Kanaun and Tkachenko, 2008). Local change in the structure could govern the properties (e.g., constriction, strut cross section, surface roughness, etc). Yet, solid foam structure and properties are still incompletely characterized [see Hugo and Topin (2012)] and hence induce many discrepancies in thermophysical properties.

There are several manufacturing routes to produce open-cell foams such as electrochemical deposition,

powder technology, casting techniques, bubbling agent technology, 3D printing, etc. In the case of existing foams (e.g., ERG, RECEMAT, ALANTUM, etc.), it has been seen that the ligament exhibits a variable cross section along its axis. In the literature, different strut shapes have been discussed that have strong influence on geometrical and thermophysical properties. On the other hand, the ligament cross section along its axis needs to be taken in account. Kanaun and Tkachenko (2008) have proposed an analytical method to calculate the effective thermal conductivity accounting the variations of convex triangular strut diameters. De Jaeger et al. (2011) have manufactured in-house open-cell aluminum foams to characterize the geometrical parameters analytically, and observed convex triangular strut shape when $\varepsilon > 0.88$. The strut diameters variation is described by a fourth-order polynomial curve along the ligament axis, where struts are thinner near the center and more material is accumulated in the vicinity of nodes.

Kelvin cellular metal foams are produced by Centre Technique des Industries de la Fonderie (CTIF) [see Dairon and Gaillard (2009)] using gravity casting with special low conductivity "sand" cores and a high metallostatic head to facilitate the infiltration of the network of struts. These authors have observed convex triangular strut shape of constant ligament cross section within a porosity range, 80–95%. Using this technique, they have reported neither circular nor concave triangular strut shapes. Most recently, Smorygo et al. (2011) have proposed an inverted spherical model based on hexagonal close packing symmetry to determine geometrical properties for ceramic foams of circular struts in the range of $0.75 < \varepsilon < 0.9$ and open-cell foams of triangular struts for $\varepsilon > 0.9$ by providing a characteristic parameter, $k = D/D_c$ (the unit cell is created by subtracting sphere of diameter, D from a cube of side, D_c). Their proposed model is not valid when $\varepsilon < 0.74$.

The strut morphology greatly influences the specific surface area and consequently the heat and mass transfer as well as pressure drop properties of the foam structures. Therefore, the accurate knowledge of the specific surface area of the foam structures is extremely important for their application in various industries. The specific surface area is an important property of foam structures, which is relevant for momentum, heat and mass transfer (e.g., Grosse et al., 2009) and hence is responsible for a successful design of structured foam reactors for single phase (e.g., Richardson et al., 2000) as well as for multiphase (e.g., Stemmet et al., 2007; Tschentscher et al., 2010; Wenmakers et al., 2010) reaction systems.

A specific surface area can be measured by various experimental techniques, namely, the Brunauer-Emmett-Teller (BET) method or magnetic resonance imaging (MRI) or image processing micro X-ray computed tomography (μCT) techniques. Depending on the pore size and material nature, one or the other method is better suited. These methods do not give the same results because they do not access the same resolution (e.g., roughness, hollow strut, etc.). In the case of a hollow strut, BET can measure surface area inside the strut. Using the μCT technique, one can separate the surface inside and outside of the hollow strut, but usually resolution is not high enough to develop the surface to account for roughness.

Apart from experiments, the models proposed by authors (Buciuman and Kraushaar-Czarnetzki, 2003; Garrido et al., 2008; Grosse et al., 2008; Moreira and Coury, 2004) to predict the specific surface area of foam structures using measured parameters such as pore or strut diameter and porosity are valid only for high porosities because of insufficient characterization of strut and node shape at lower porosities. As foam characteristics and pressure drop are greatly affected by the interface geometry, accurate estimation of specific surface area a_c is critically important. Edouard et al. (2008) have plotted the calculated values of various authors as dimensionless product $a_c d_p$ (product of specific surface area and pore diameter) versus the foam porosity (ε). They have shown that independent of the pore size, the evolution of the specific surface area as a function of the foam porosity follows two different behaviors. For a group of authors, $a_c d_p$ increases linearly with porosity increase while for a group of authors, $a_c d_p$ decreases by a factor ranging between 2 and 4 according to the correlation used. The reason for such discrepancies in the literature is probably due to consideration of oversimplified geometry of the unit cell. Moreover, many authors (e.g., Buciuman and Kraushaar-Czarnetzki, 2003; Garrido et al., 2008; Grosse et al., 2008; Moreira and Coury, 2004) have measured only one of the geometrical properties (either pore diameter or porosity, or specific surface area or strut diameter) and then calculated other parameters using their analytical models. In order to avoid bias in measuring geometrical properties on existing samples, Brun et al. (2009) have measured simultaneously several geometrical properties of different foams, namely, Recemat and ERG of different porosities using iMorph [see Brun et al. (2008)] and provided a database.

There is no way to know before the end that a particular correlation is applicable or not to determine geometrical properties. All correlations work pretty well for

a given set of foams, but they fail for other foams. The reasons of failure of the correlations reported in the literature could be (i) the lack of adapted input parameters, (ii) a presupposed relationship between parameters, and (iii) the difficulty to obtain foam samples with individually varied morphological parameters. For example, the porosity of commercially available foams (with the same global structure) is nearly fixed ($\varepsilon \sim 90\% \pm 3\%$).

Very few works in the literature deal with strut shape influence on geometrical properties and thermophysical ones, e.g., Kanaun and Tkachenko (2008) and De Jaeger et al. (2011) have proposed a generic expression that accommodates strut cross-sectional variation from convex triangular to concave triangular and eventually to circular.

To our knowledge, no one studied different strut cross sections like circular, square, diamond (double equilateral triangle), hexagon, and star. Recently, it has become possible to produce foam structures with such cross sections using 3D printing or rapid prototyping. The majority of commercially existing foams are, in fact, composed of slightly elongated Kelvin-like cells.

In this paper, we focus on the simplest case of isotropic foam structure of Kelvin-like cell because it is the simplest representative a periodic unit cell. Homothetic transform of unit cell influence on morphological (and thermos-hydraulic) parameters is known. We choose to fix d_{cell} and vary strut shapes, which consequently varies the geometrical properties by changing porosity ε. At constant d_{cell}, we can change ε by controlling d_{s}, which allows us to study the individual influence on porosity. Moreover, changing the strut cross section at constant d_{cell} allows us to study its influence on porosity and its impact on various geometrical properties.

We have generated virtual Kelvin-like foams having strut shapes from simple circular geometry to the complex geometry of star (regular hexagram) for a constant ligament cross section. Using computer aided design (CAD) modeling, we are able to generate different strut shapes of constant cross section for a wide range of porosity ($0.60 < \varepsilon < 0.95$). The objective is to study the effect of individual parameters such as strut shape, porosity, etc., on foam geometry (and ultimately on thermophysical properties) to understand which parameters impact strongly on foam geometry. This work aims to develop accurate correlations (based on the tetrakaidecahedron geometry and different strut morphologies of the foam structures) for the theoretical estimation of all geometrical properties of any kind of foams that are applicable to different foam materials and porosities and can be valid for a wide range of existing foams.

Moreover, these correlations can provide insight to tailor one's own foam accordingly to apply them in various industrial applications. In this way, one can realize any number of foams depending on the various engineering applications. Three-dimensional image processing is used to classify strut diameter, pore diameter, porosity, and specific surface area of different foams.

2. CHARACTERIZATION OF FOAMS

2.1 Geometrical Modeling

We have generated simple strut shapes like circular, diamond (double equilateral triangle), square, hexagon, and star (regular hexagram). Their cross sections are in line with the ligament axis of the truncated octahedron edge. Moreover, we have studied the rotation of square and hexagon shapes at 45 and 90 deg, respectively, with respect to the ligament axis where the node forms a quite different shape from the original ones, which has a subsequent effect on geometrical properties. Moreover, the same shapes with and without rotation also greatly influence thermos-hydraulic properties. Note that we have considered a constant cross section of the ligament.

In CAD modeling, we have first started with a tetrahedral element composed of four identical half struts. This choice of a structural element is consistent with the topological feature of foam. We then model 3D foam with this smallest repetitive element, which defines a spatially periodic structure. Microstructural features of open-cell foam are represented by a tetrahedral unit cell with a skeleton of four half struts of length $L/2$, where the dihedral angle is approximately 109.471 deg at edges shared by two hexagons or 125.263 deg at edges shared by a hexagon and a square (see Fig. 4 in Section 3.1). Figure 1 shows the construction of a Kelvin cell, which is based on a truncated octahedron (left and right). The node-to-node length ($L = 2$ mm) is kept fixed for entire calculations, which is based on the fixed cell diameter (d_{cell}).

For every strut shape, we have followed the same procedure of creating four half struts followed by replication to create a unit cell. Figure 2 shows the different shapes and their characteristics dimensions for a given porosity.

2.2 CAD Calculations

We have defined a construction method that allows us to use strut shape and porosity as control parameters. Using our construction method, we can generate foams of chosen porosity for any strut shape. Due to the chosen

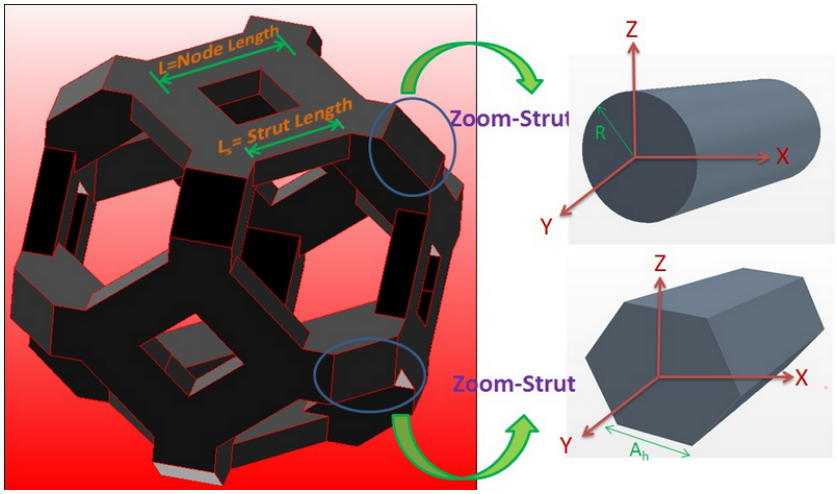

FIG. 1: Presentation of tetrakaidecahedon model of Kelvin cell (left). Strut length L_s and node-to-node length L are clearly shown. Constant cross section of ligament with different strut shapes, circular (on the top-right) and hexagon (at the bottom-right), are presented with their characteristic dimension.

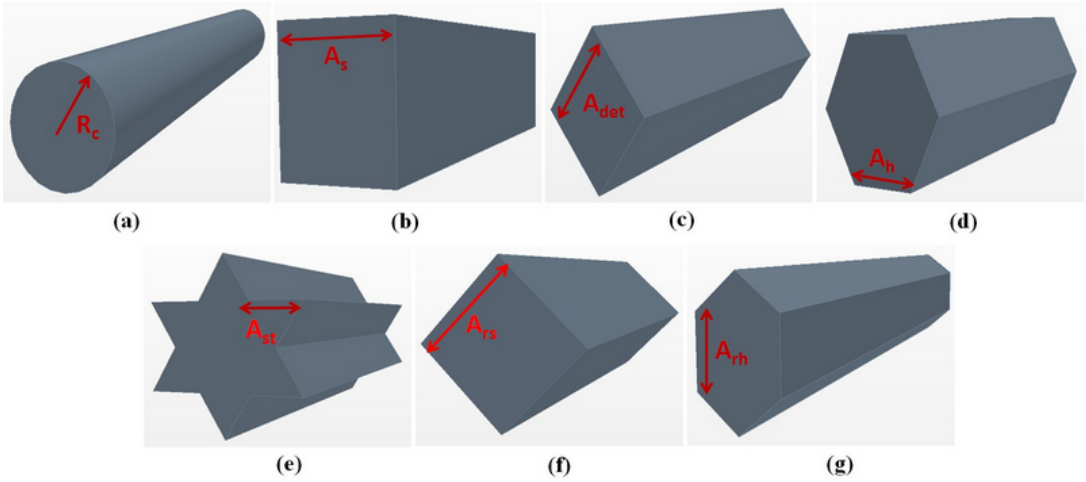

FIG. 2: Representation of different 3D strut and ligament shapes: **(a)** circular, **(b)** square, **(c)** diamond (double equilateral triangle), **(d)** hexagon, **(e)** star, **(f)** rotated square, **(g)** rotated hexagon. The characteristic dimensions are also presented that are used in Section 3.1 and Appendices A and B for analytical solutions.

construction method, some limitations rise, mainly for the complex shapes (e.g., diamond, star). Our procedure creates only (in a periodic unit cell) 36 struts that are along the edge of the truncated octahedron. For certain shapes and values of porosity, mainly for low porosities, some other strut part has to be added in the unit cell, which limits our procedure.

We have measured all geometrical parameters of 45 virtual Kelvin-like foams using the classical approach (see Table 1). We have generated porosities for circular, square, hexagon, and rotated hexagon down to 60%, for diamond and rotated square strut shapes down to 80% and down to 75% for star strut shapes. We have also presented square and hexagon face window area, a_{sw} and a_{hw}. The equivalent window area of square and hexagon face based on strut length are also presented (see Table 1) and detailed in Section 3.1. Note that α_{eq} and β in Table 1 are described in Section 3.1.

Figure 3 represents Kelvin-like cell foams of different strut shapes inside a cube where struts accumulate the

TABLE 1: Values of various strut shapes, porosities, and their characteristic dimensions

			CAD measurement			Analytical				
Shape	ε **(%)**	d_s **or** A **(mm)**	a_{sw} **(mm^2)**	a_{hw} **(mm^2)**	a_c **(m^{-1})**	$\alpha_{\mathrm{eq}} = R_{\mathrm{eq}}/L$	$\beta = L_{\mathrm{s}}/L$	a_{sw} **(mm^2)**	a_{hw} **(mm^2)**	a_c **(m^{-1})**
Circular	60	1.212	0.198	0.514	982	0.429	0.341	0.232	0.603	1037
	65	1.110	0.277	0.720	979	0.392	0.393	0.309	0.803	1020
	70	1.006	0.371	0.965	960	0.356	0.447	0.400	1.039	992
	75	0.900	0.482	1.252	926	0.318	0.504	0.507	1.318	949
	80	0.789	0.614	1.595	873	0.279	0.563	0.635	1.649	889
	85	0.669	0.773	2.009	796	0.236	0.628	0.790	2.052	807
	90	0.534	0.975	2.533	686	0.189	0.702	0.987	2.564	692
	95	0.367	1.255	3.261	515	0.130	0.794	1.262	3.279	518
Square	60	1.075	0.197	0.511	1092	0.760	0.341	0.232	0.603	1122
	65	0.984	0.277	0.720	1091	0.696	0.393	0.309	0.803	1111
	70	0.891	0.372	0.965	1074	0.630	0.447	0.400	1.039	1085
	75	0.797	0.483	1.255	1037	0.563	0.504	0.507	1.318	1043
	80	0.698	0.615	1.598	979	0.493	0.563	0.635	1.649	982
	85	0.591	0.775	2.014	895	0.418	0.628	0.790	2.052	895
	90	0.472	0.977	2.538	772	0.334	0.702	0.987	2.564	771
	95	0.325	1.257	3.266	580	0.229	0.794	1.262	3.279	579
Rotated Square	80	0.694	0.632	1.649	996	0.491	0.563	0.635	1.649	1050
	85	0.589	0.788	2.052	906	0.416	0.628	0.790	2.052	944
	90	0.470	0.982	2.564	779	0.332	0.702	0.987	2.564	803
	95	0.324	1.261	3.279	583	0.229	0.794	1.262	3.279	594
Diamond	80	0.752	0.623	1.619	1070	0.532	0.563	0.635	1.649	1043
	85	0.637	0.779	2.024	974	0.450	0.628	0.790	2.052	953
	90	0.508	0.977	2.538	838	0.359	0.702	0.987	2.564	823
	95	0.349	1.254	3.259	627	0.247	0.794	1.262	3.279	620
Hexagon	60	0.665	0.199	0.517	1025	0.470	0.341	0.232	0.603	1070
	65	0.609	0.279	0.725	1023	0.431	0.393	0.309	0.803	1056
	70	0.552	0.373	0.970	1005	0.390	0.447	0.400	1.039	1028
	75	0.494	0.484	1.258	970	0.349	0.504	0.507	1.318	986
	80	0.432	0.616	1.602	915	0.306	0.563	0.635	1.649	925
	85	0.367	0.776	2.016	835	0.259	0.628	0.790	2.052	841
	90	0.292	0.977	2.539	720	0.207	0.702	0.987	2.564	723
	95	0.201	1.257	3.267	540	0.142	0.794	1.262	3.279	542
Rotated Hexagon	60	0.664	0.202	0.525	1033	0.469	0.341	0.232	0.603	1070
	65	0.608	0.282	0.733	1029	0.430	0.393	0.309	0.803	1056
	70	0.551	0.377	0.978	1009	0.390	0.447	0.400	1.039	1028
	75	0.493	0.488	1.267	973	0.348	0.504	0.507	1.318	986
	80	0.432	0.620	1.611	917	0.305	0.563	0.635	1.649	925
	85	0.366	0.779	2.025	837	0.259	0.628	0.790	2.052	841
	90	0.292	0.980	2.547	721	0.207	0.702	0.987	2.564	723
	95	0.201	1.260	3.273	541	0.142	0.794	1.262	3.279	542
Star	75	0.347	0.489	1.270	1399	0.246	0.504	0.507	1.318	1306
	80	0.305	0.620	1.611	1314	0.215	0.563	0.635	1.649	1240
	85	0.258	0.779	2.023	1195	0.183	0.628	0.790	2.052	1140
	90	0.206	0.979	2.545	1027	0.146	0.702	0.987	2.564	991
	95	0.142	1.258	3.269	769	0.100	0.794	1.262	3.279	751

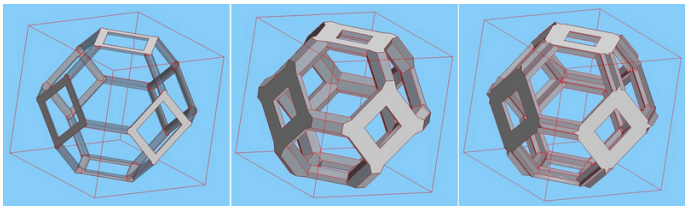

FIG. 3: Presentation of 3D circular, hexagon, and star strut shape virtual Kelvin-like cell foams inside a periodic cubic unit cell. The struts belonging to square faces and all nodes are shared by two unit cubic cells. The 12 other struts are fully included in the cubic cell.

edges of the truncated octahedron and we keep only the struts that are totally included in the truncated octahedron and the cubic cell. The length of the cubic cell is $2\sqrt{2}L$.

3. ANALYTICAL APPROACH

Generally, many authors (e.g., Bhattacharya et al., 2002; Calmidi, 1998; Du Plessis et al., 1994; Inayat et al., 2011) have measured three morphological parameters, either d_s or d_p or ε, and used them to describe other foam properties based on their simple representative unit cell by adjusting the shape parameters using a regular network model. In order to accommodate different shapes proposed by various authors (Bhattacharya et al., 2002; Buciuman and Kraushaar-Czarnetzki, 2003; De Jaeger et al., 2011; Garrido et al., 2008; Grosse et al., 2009; Inayat et al.; 2011; Moreira and Coury, 2004), we have introduced other complex shapes to study their impact and characterize their geometrical parameters. The analytical approach is carried out for an isotropic periodic Kelvin cell, as shown in Fig. 1.

3.1 Geometrical Parameters

The Kelvin cell is associated with a minimization of surface area for a given cell volume and the physics of foam leads to the formation of a concave triangular shape, which has been studied for a century. Due to Plateau's law, the natural strut shape is usually convex or concave triangle. Classical replication techniques lead usually to a triangular or circular strut cross section. Using a casting technique or rapid prototyping or 3D printing gives access to produce virtually any other strut shapes. Dairon and Gaillard (2009) have manufactured constant strut shapes (convex triangular) using a casting process for a porosity range of 80–95% for constant ligament cross sections.

The node junction at different porosities and different strut shapes possesses complex shape and is difficult to visualize. To make our analytical approach clear and user-friendly, we have approximated the shapes at the junctions because different strut shapes behave differently at the junction. Moreover, it is very difficult to derive exact calculations for each strut shape. As circular shape is easy to visualize at the node and does not possess complex geometry compared to other strut shapes, we have defined an equivalent radius, R_{eq}, for different shapes that are provided in Table 2.

For each porosity and different strut shape, we have assumed an equivalent radius, which is the radius of the circle of the same area as the strut cross section. Obviously, for a given R_{eq}, the node volume is the same and independent of the strut shape. It is the most important hypothesis in our derivation.

In order to provide an approximate analytical solution, we have defined L_s as the strut length (without considering node points) and L as the distance between two nodes (or length of solid truncated octahedron edge) as shown in Fig. 1. For any strut shape, we have considered an equivalent circular shape of radius R_{eq} and then deduced its characteristic dimensional dependence of different shapes as provided in Table 2.

We chose to base our node volume calculation on that given by Kanaun and Tkachenko (2008). The volume of a node at the junction of four struts of equivalent circular shape is given as (see Fig. 4)

$$V_{\text{node}} = \underbrace{4}_{\text{Four pyramids}} \times \underbrace{\frac{1}{3}\pi R_{\text{eq}}^2}_{\text{Base area of a pyramid}} \times \underbrace{R_{\text{eq}}}_{\text{Height of the pyramid}} = \frac{4}{3}\pi R_{\text{eq}}^3 \tag{1}$$

Volume of the ligament of equivalent circular shape is given as

$$V_{\text{ligament}} = \pi R_{\text{eq}}^2 L_s \tag{2}$$

TABLE 2: Representation of characteristic length, symbol, and equivalent radius of various strut shapes

Shapes	Characteristic length	Characteristic symbol	Equivalent radius
Circular	Radius	R_c	$R_{\text{eq}} = R_c$
Square	Length of the side	A_s	$R_{\text{eq}} = A_s/\sqrt{\pi}$
Rotated Square (at 45°)	Length of the side	A_{rs}	$R_{\text{eq}} = A_{\text{rs}}/\sqrt{\pi}$
Diamond	Length of the side	A_{det}	$R_{\text{eq}} = A_{\text{det}}\sqrt{\sqrt{3}/2\pi}$
Hexagon	Length of the side	A_h	$R_{\text{eq}} = A_h\sqrt{3\sqrt{3}/2\pi}$
Rotated Hexagon (at 90°)	Length of the side	A_{rh}	$R_{\text{eq}} = A_{\text{rh}}\sqrt{3\sqrt{3}/2\pi}$
Star (regular Hexagram)	Length of the side	A_{st}	$R_{\text{eq}} = A_{\text{st}}\sqrt{3\sqrt{3}/\pi}$
*Equilateral Triangle	Length of the side	A_t	$R_{\text{eq}} = A_t\sqrt{\sqrt{3}/4\pi}$

*R_{eq} for equilateral triangular strut presented here is used for validation in Section 4.

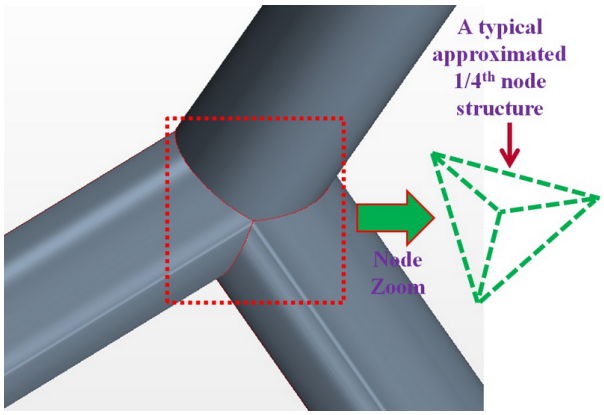

FIG. 4: A typical node of foam structure. We have shown the four faces of a pyramid that is taken into consideration in calculating the volume of the node. The face of the nodes changes with the strut shape. We have shown four struts of circular shape at the node, which is approximated as triangular pyramid. (Zoom-node represents one pyramid here, but for calculation, we accounted for four pyramids to determine a node for four struts).

At the node junction, we can approximate the node by using geometrical interpretation as (shown in Fig. 4)

$$1.6R_{\text{eq}} + L_s = L \tag{3}$$

In dimensionless form, we can rewrite Eq. (3) as

$$1.6\alpha_{\text{eq}} + \beta = 1 \tag{4}$$

where $\alpha_{\text{eq}} = R_{\text{eq}}/L$ and $\beta = L_s/L$.

Total volume of a truncated octahedron is given as

$$V_T = 8\sqrt{2}L^3 \tag{5}$$

In a truncated octahedron structure (see Fig. 1, left), there are 36 ligaments and 24 nodes but only 1/3 of both, volume of ligament and volume of node is included in the unit periodic cell.

For a periodic Kelvin-like cell foam in a unit cell, solid volume V_s is given as

$$V_s = \frac{1}{3}\left(36V_{\text{ligament}} + 24.V_{\text{node}}\right) \tag{6}$$

Porosity of a porous medium is given as

$$\varepsilon = \frac{V_T - V_s}{V_T} \tag{7}$$

Equations (5)–(7) represent a general methodology to evaluate the geometrical properties of the equivalent circular shape of metal foam. We have shown one of the studied shapes and the correlation between geometrical parameters, say, for circular strut shape, $R_{\text{eq}} = R_c$.

On substitution, we get

$$\varepsilon = 1 - \frac{\frac{1}{3}\left(36\pi R_c^2 L_s + 24.\frac{4}{3}\pi R_c^3\right)}{8\sqrt{2}L^3}$$
$$\Rightarrow 12\pi\alpha_c^2\beta + \frac{32}{3}\pi\alpha_c^3 = 8\sqrt{2}\left(1-\varepsilon\right) \tag{8}$$

where $\alpha_c = R_c/L$ and $\beta = L_s/L$

Note that α_c is the ratio of strut radius to node length where subscript c represents circular shape. Moreover, β is found to be independent of strut shape.

For all the other strut shapes, we have presented the relation between porosity and geometrical parameters in Appendix A. Equation (8) gives the generic relation of porosity as a function of geometrical parameters.

We could combine Eqs. (4) and (8) to get approximate values of α_{eq} and β as a function of ε. This approach can be used to determine all the geometrical properties if a full set of geometrical parameters are not known. We have plotted different values of α_{eq} and β for different shapes, which clearly follow a power law as shown in Figs. 5 and 6 and can be expressed as

$$\alpha_{eq} = \chi\,(1-\varepsilon)^{\psi} \tag{9}$$

$$\beta = 1 - 1.6\,\chi\,(1-\varepsilon)^{\psi} \tag{10}$$

where χ and ψ are the parameters that depend not only on strut shape but also on rotation but with less impact (as the node shape changes little with strut rotation, the parameters χ and ψ are influenced).

From Fig. 5, it is clearly seen that the α_{eq} follows the same trend of power law with respect to porosity where the exponent of power law is always <1. There are nearly three groups of α_{eq} that mainly depend on strut shape. One group, which has higher α_{eq}, is that of diamond, square, and rotated square strut shapes. The second group is that of hexagon, rotated hexagon, and circular strut shapes. The third group is that of star shape, which has the lowest α_{eq}. In Fig. 6, we have obtained a unique curve of β for all the strut shapes. It is mainly due to the hypothesis that foam samples possess the same node volume irrespective of the strut shape.

3.2 Specific Surface Area

As it is far more convenient to calculate the specific surface area using a cubic unit cell, we consider the foam shape in the cubic cell of volume V_c (see Fig. 3), and the specific surface area a_c can be written as

$$a_c = \frac{(36\,S_{\text{ligament}} + 24 S_{\text{node}})}{V_c} \tag{11}$$

where S_{ligament} and S_{node} are the surface area of one ligament and node contained in the cubic cell of volume V_c (the distance between two opposite points is $2\sqrt{2}L$ and thus, $V_c = 2V_T$).

In Fig. 3, we have presented Kelvin-like cell foams in a cubic cell of different strut shapes. One can easily notice that there are 12 full ligaments and 24 half ligaments in a unit cell. Also, at the node junction, there are two half nodes and one one-fourth node.

Specific surface area of a circular strut shape is given as

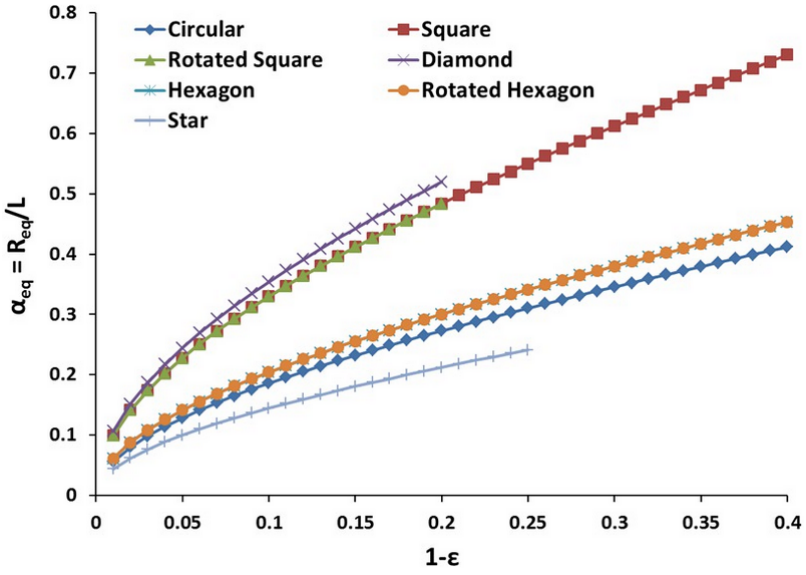

FIG. 5: Plot of α_{eq} versus $1-\varepsilon$. α_{eq} for different strut shapes is limited with respect to porosity as per construction methodology.

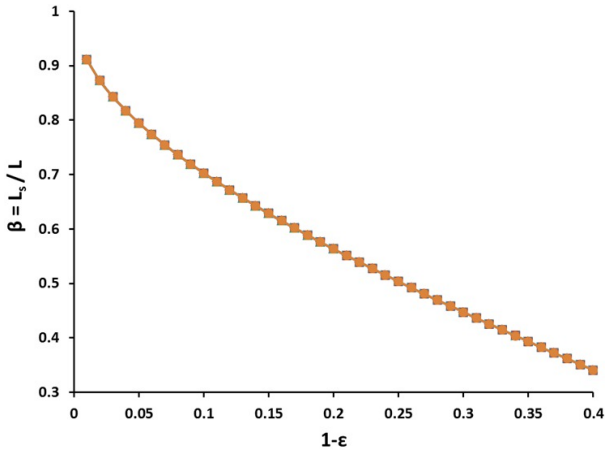

FIG. 6: Plot of β versus $1-\varepsilon$. A unique curve is obtained for all the strut shapes due to the hypothesis made.

$$a_c = \frac{\left\{48\pi R_c L_s + 24.\frac{3}{4}\left(\frac{5}{4}\pi R_c^2\right)\right\}}{2\left(8\sqrt{2}L^3\right)} = \frac{1}{\sqrt{2}L}\left(3\pi\alpha_c\beta + \frac{45}{32}\pi\alpha_c^2\right) \quad (12)$$

For all the other strut shapes, we have presented the relation between specific area, node length, and geometrical parameters in Appendix B.

For a given unit cell, the node length is fixed and one can easily determine the specific surface area of different strut shapes. We have presented a nondimensional curve $a_c L$ with respect to porosities in Fig. 7. From this curve, one can identify either a_c or L for a known porosity. While keeping the same porosity, one can increase the specific surface area by utilizing different strut shapes. The maximum increase in specific area is observed for the star strut shape while the lowest is observed for the circular strut shape. Moreover, a gradual increase of 25% at low porosity ($\varepsilon \approx 60\%$) up to 60% at moderate porosity ($\varepsilon \approx 75\%$) in specific surface area is noticed from the circular to star strut shape.

We have also presented a nondimensional curve relating $\alpha_{eq} a_c$ with porosity in Fig. 8. Using this curve, one can characterize all the geometrical parameters of any strut shape. If any of the one or two quantities are known, one can easily determine all the geometrical parameters using the above established correlations and curves. Moreover, these correlations can be used to determine the shape of the strut for a given $\alpha_{eq} a_c$, which can give one insight to tailor their own foam ac-

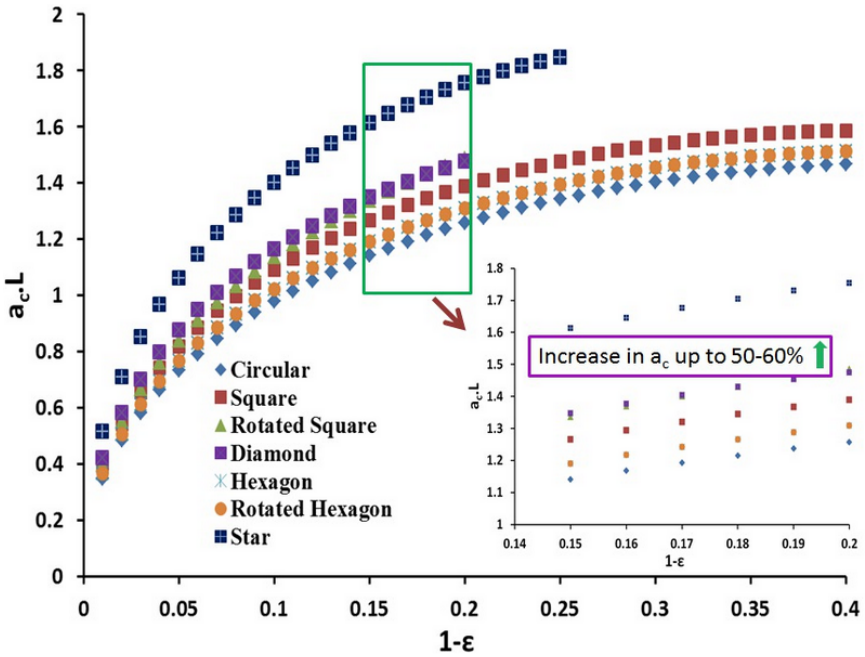

FIG. 7: Plot of $a_c L$ (dimensionless) versus $1-\varepsilon$. A sharp increase in a_c is observed at lower porosity for complex shapes.

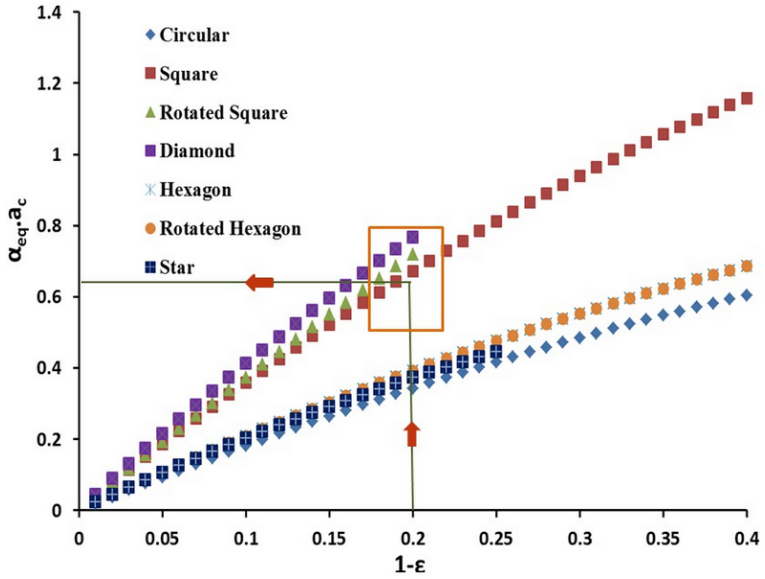

FIG. 8: Plot of $\alpha_{eq}.a_c$ (nondimensional) versus $1-\varepsilon$. For a given application purpose of $\varepsilon > 0.80$ (mechanical constraint) and hydraulic constraint ($\alpha_{eq}.a_c > 0.6$), only square, rotated square, or diamond shape can be used.

cordingly. In this way, one can realize any number of foams depending on the various engineering applications needs.

We present an algorithm in Fig. 9 to determine relations and values of all geometrical parameters of any given shape if any of the two geometrical parameters, namely, d_s or A_{side}, and L are known. It is not always necessary to have prior information about d_s or A_{side} and L. For instance, if any of the two foam geometrical properties are known, one can easily characterize other geometrical properties using Figs. 5–8 and correlations. Moreover, these curves and correlations are useful depending on the industrial applications. For a known output, one can deduce all the input geometrical parameters for a given application.

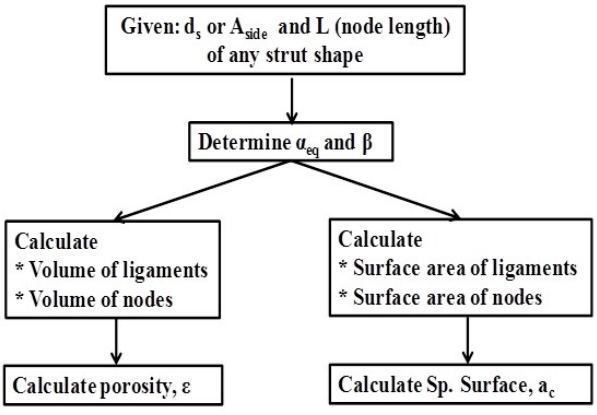

FIG. 9: Algorithm to calculate porosity and specific surface area.

4. VALIDATION

In order to validate the proposed analytical model, data obtained on virtual CAD samples and experimental data are compared and found to be in excellent agreement. For CAD samples, we have compared strut diameter and the specific surface area of the different shapes for a given node length for all porosities.

From Fig. 10, the bias in the strut diameters is observed up to 3% because of geometrical approximations taken on the struts node connection and the analytical d_s is underestimated. The comparison of specific surface area obtained by classical method (see Table 1) and an analytical approach is presented in Fig. 11. The errors are within ±3% for various shapes but in the case of star strut shape, the specific surface area is underestimated by 6% only at low porosities. One of the reasons is the complex nature of the microstructural node for complex shapes (e.g., star) at low porosities.

Very few works in the literature exist with complete measurement of all geometrical properties. Moreover, the literature on experimental determination of geometrical properties may include bias linked to the "tools" used

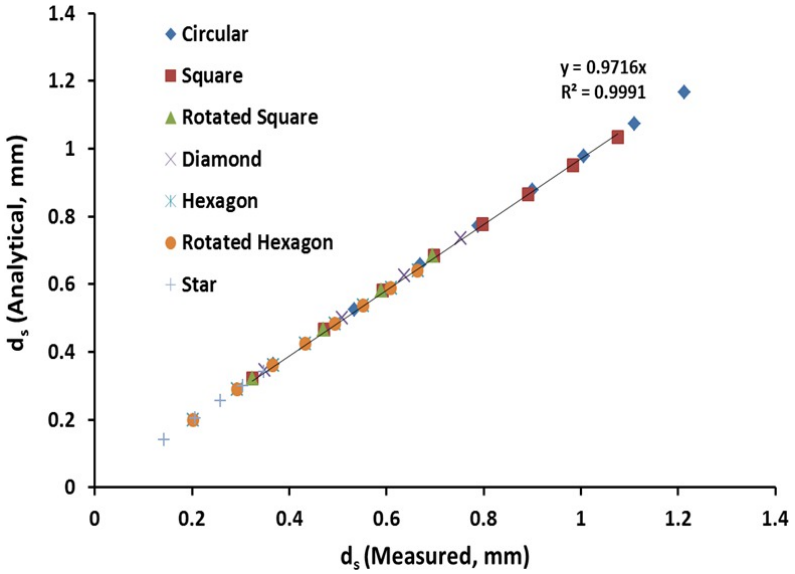

FIG. 10: Validation of strut diameter (or side length) of various shapes by classical measurement and analytical approach.

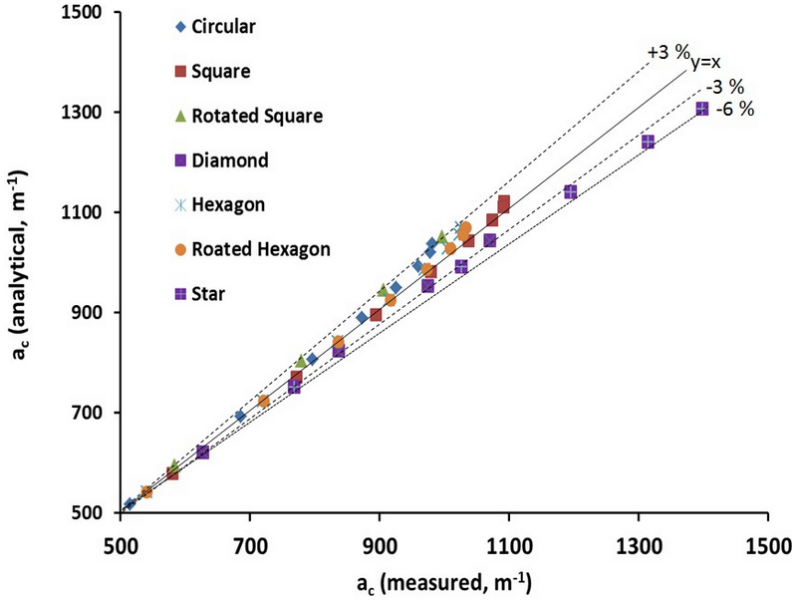

FIG. 11: Validation of specific surface areas of various strut shapes by classical measurement and analytical approach.

to measure geometrical parameters. In order to maintain a consistency in measuring the parameters, Brun et al. (2008) have developed an in-house code, iMorph, to measure all geometrical parameters of their foams [see Brun et al. (2009)]. Their definition to measure pore diameter is based on equivalent included spherical diameter in the foam structure. They have measured geometrical properties on Recemat (nickel-chromium alloy), ERG (Al foams), and Fibernide (Ni foams). De Jaeger et al. (2011) and Perrot et al. (2007) have measured geometrical parameters of their PU foams based on cell diameters that are orthotropic in nature and possess convex triangular strut shape. This yields 17 (Al/NC/Ni/PU) open-cell foam samples, presented in Table 3, allowing validation of

TABLE 3: Comparison of specific surface area by measured data and data reported in the literature

	Data from direct measurement				Analytical approach				
Authors	Samples	ε	d_p (μm)	a_c (m^{-1})	α_{eq}	β	L (μm)	a_c (m^{-1})	Error (%)
Brun et al. (2009)	Recemat NC1116	89.6	2452	1300	0.4575	0.7283	913	1259	–3.15
	Recemat NC1723	87.3	1840	1740	0.5037	0.7008	691	1786	2.64
	Recemat NC2733	90.9	831	4288	0.429	0.7452	270	4061	–5.29
	Recemat NC3743	87.3	569	5360	0.5037	0.7008	233	5299	–1.14
	ERG Al 10	89.2	4497	558	0.4721	0.7196	1780	626	12.19
	ERG Al 20	88.9	3969	549	0.4659	0.7233	1920	607	10.56
	ERG Al 40	88.5	3442	743	0.4802	0.7148	1480	805	8.34
	Fibernide Ni10	89.5	4429	718	0.4597	0.727	1650	699	–2.65
De Jaeger et al. (2011)	PPI 10	93.2	2540	440	0.3726	0.7787	2203	446	1.36
	PPI 10	95.1	2540	380	0.3177	0.8113	2270	381	0.26
	PPI 20	91.3	1270	860	0.4198	0.7506	1336	807	–6.16
	PPI 20	93.7	1270	720	0.3590	0.7867	1467	650	–9.72
	PPI 20	96.7	1270	580	0.262	0.8444	1297	565	–2.59
Perrot et al. (2007)	PPI 5	91.8	5080	431	0.408	0.7577	2312	456	5.80
	PPI 10	91.8	2540	478	0.408	0.7577	2326	453	–5.23
	PPI 20	91.7	2540	624	0.4104	0.7563	1641	646	3.53
	PPI 40	92.3	2540	700	0.3957	0.7649	1393	736	5.14
	Avg. Deviation								0.82

*Pore diameter d_p of gray blocks (samples in PPI) are estimated as $d_p = 25.4/\text{PPI}$.

our geometrical model. Note that we have not constructed any triangular strut shape in our study because the literature includes a large number of models associated with this shape. For validation, we have assumed the samples of De Jaeger et al. (2011) and Perrot et al. (2007) as quasi isotropic.

For all the 17 samples, their strut shapes are found to be either convex triangular or equilateral triangle type. We have approximated the strut shape as equilateral triangle, and using the methodology of equivalent radius R_{eq} presented in Section III.A (see Table 2), we have compared the specific surface area of 17 samples, and the errors associated with them are enlisted in Table 3. We have used ε to calculate α_{eq} and β followed by determining node length L using d_p.

In Fig. 12, it is obvious that the proposed analytical model is in good agreement with the measured and experimental specific surface areas within an error range of ±6%. The reason to compare different foams to our proposed model is to increase the scope of model validity over a wide range of different strut shapes of different materials and different manufacturing techniques.

5. CONCLUSION

Virtual foams of different strut shapes along with their orientations using CAD modeling are tailored in the porosity range 60–95%. The proposed correlations have been derived for constant cross section of ligament for different strut shapes. The final outcome from the proposed model is very effective. A very good agreement between the predicted results and the available experimental data has also been observed.

It should be noted that experimental or image processing data of variable cross section of ligaments with different strut shapes for a wide range of porosity are still unavailable to our knowledge. However, further experimental data with different varied ligament cross section of strut shapes would be welcome in order to give better support to the proposed model, and this will be the subject of a future article.

ACKNOWLEDGMENT

The authors express their gratitude to ANR (Agence Nationale de la Recherche) for financial support in the

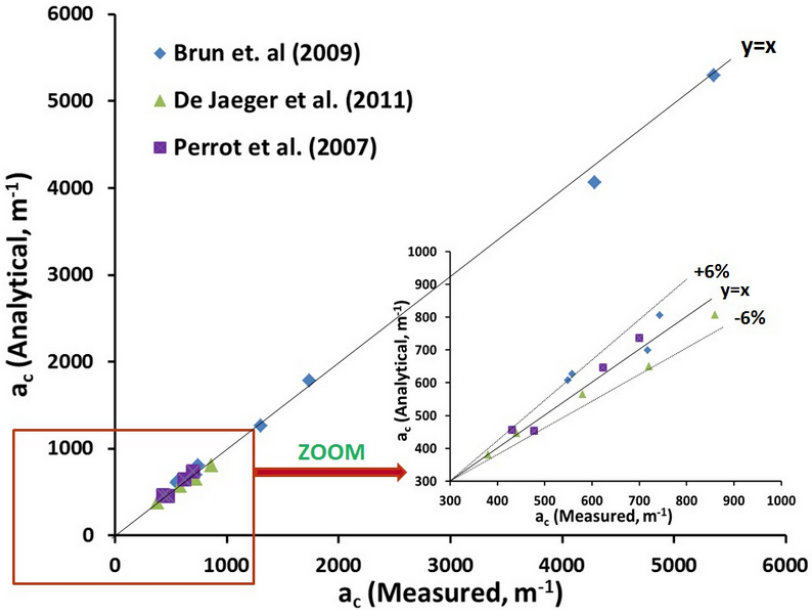

FIG. 12: Comparison of analytical and measured values of specific surface area. Globally, all data points lie within ±6%.

framework of FOAM project and all project partners for their assistance.

REFERENCES

Avenall, R. J., Use of Metallic Foams for Heat Transfer Enhancement in the Cooling Jacket of a Rocket Propulsion Element, Master's thesis, University of Florida, 2004.

Bhattacharya, A., Calmidi, V. V., and Mahajan, R. L., Thermophysical Properties of High Porosity Metal Foams, *Int. J. Heat Mass Transfer*, vol. **45**, no. 5, pp. 1017–1031, 2002.

Brun, E., Vicente, J., Topin, F., and Occelli, R., iMorph: A 3D Morphological Tool to Fully Analyse All Kind of Cellular Materials, Cellmet Conference, Dresden, 2008.

Brun, E., Vicente, J., Topin, F., Occelli, R., and Clifton, M. J., Microstructure and Transport Properties of Cellular Materials: Representative Volume Element, *Adv. Eng. Mat*., vol. **11**, no. 10, pp. 805–810, 2009.

Buciuman, F. C. and Kraushaar-Czarnetzki, B., Ceramic Foam Monoliths as Catalyst Carriers. 1. Adjustment and Description of the Morphology, *J. Ind. Eng. Chem. Res*., vol. **42**, pp. 1863–1869, 2003.

Calmidi, V. V., Transport Phenomena in High Porosity Metal Foams, Ph.D. Thesis, University of Colorado, 1998.

Dairon, J. and Gaillard, Y., Casting Parts with CTIF Foams, MetFoam Conference, Slovakia, 2009.

De Jaeger, P., T'Joen, C., Huisseune, H., Ameel, B., and De Paepe, M., An Experimentally Validated and Parameterized Periodic Unit-Cell Reconstruction of Open-Cell Foams, *J. Appl. Phys*., vol. **109**, no. 10, p. 103519, 2011.

Du Plessis, P., Montillet, A., Comiti, J., and Legrand, J., Pressure Drop Prediction for Flow through High Porosity Metallic Foams, *Chem. Eng. Sci*., vol. **49**, no. 21, pp. 3545–3553, 1994.

Edouard, D., Lacroix, M., Huu, C. P., and Luck, F., Pressure Drop Modeling on Solid Foam: State-of-the-Art Correlation, *Chem. Eng. Sci*., vol. **144**, no. 2, pp. 299–311, 2008.

Garrido, G. I., Patcas, F. C., Lang, S., and Kraushaar-Czarnetzki, B., Mass Transfer and Pressure Drop in Ceramic Foams: A Description of Different Pore Sizes and Porosities, *Chem. Eng. Sci*., vol. **63**, no. 21, pp. 5202–5217, 2008.

Giani, L., Groppi, G., and Tronconi, E., Mass-Transfer Characterization of Metallic Foams as Supports for Structured Catalysts, *Ind. Eng. Chem. Res*., vol. **44**, no. 14, pp. 4993–5002, 2005a.

Giani, L., Groppi, G., and Tronconi, E., Heat Transfer Characterization of Metallic Foams, *Ind. Eng. Chem. Res*., vol. **44**, no. 24, pp. 9078–9085, 2005b.

Gibson, L. J. and Ashby, M. F., Cellular Solids: Structure and Properties, Second Edition, Cambridge University Press, Cambridge, UK, 1997.

Grosse, J., Dietrich, B., Martin, H., Kind, M., Vicente, J., and Hardy, E. H., Volume Image Analysis of Ceramic Sponges,

J. Chem. Eng. Tech., vol. **2**, pp. 307–314, 2008.

Grosse, J., Dietrich, B., Incera Garrido, G., Habisreuther, P., Zarzalis, N., Martin, H., Kind, M., and Kraushaar-Czarnetzki, B., Morphological Characterization of Ceramic Sponges for Applications in Chemical Engineering, *Ind. Eng. Chem. Res*., vol. **4**, no. 23, 10395–10401, 2009.

Hugo, J.-M., and Topin, F., Metal Foams Design for Heat Exchangers: Structure and Effectives Transport Properties, *Heat Mass Trans. Porous Media*: *Adv. Struct. Mater*., vol. **13**, pp. 219–244, 2012.

Inayat, A., Freund, H., Zeiser, T., and Schwieger, W., Determining the Specific Surface Area of Ceramic Foams: The Tetrakaidecahedra Model Revisited, *Chem. Eng. Sci*., vol. **66**, no. 6, pp. 1179–1188, 2011.

Jang, W. Y., Kraynik, A. M., and Kyriakides, S., On the Microstructure of Open-Cell Foams and Its Effect on Elastic Properties, *Int. J. Solids Struct*., vol. **45**, pp. 1845–1875, 2008.

Jung, A., Natter, H., Diebels, S., Lach, E., and Hempelmann, R., Nano-Nickel Coated Aluminum Foam for Enhanced Impact Energy Absorption, *Adv. Eng. Mater*., vol. **13**, no. 1-2, pp. 23–28, 2011.

Kanaun, S. and Tkachenko, O., Effective Conductive Properties of Open-Cell Foams, *Int. J. Eng. Sci*., vol. **46**, pp. 551–571, 2008.

Kim, S. Y., Paek, J. W., and Kang, B. H., Flow and Heat Transfer Correlations for Porous fi in Plate-fii Heat Exchanger, *J. Heat Transfer*, vol. **122**, no. 3, pp. 572–578, 2000.

Lafdi, K., Mesalhy, O., and Shaikh, S., Experimental Study on the Influence of Foam Porosity and Pore Size on the Melting of Phase Change Materials, *J. Appl. Phys*., vol. **102**, p. 083549, 2007.

Losito, O., An Analytical Characterization of Metal Foams for Shielding Applications, *PIERS Online*, vol. **4**, pp. 805–810, 2008.

Lu, T. J., Stone, H. A., and Ashby, M. F., Heat Transfer in Open-Cell Metal Foams, *Acta Mater*., vol. **46**, no. 10, pp. 3619–3635, 1998.

Moreira, E. A. and Coury, J. R., The Influence of Structural Parameters on the Permeability of Ceramic Foams, *Braz. J. Chem. Eng*., vol. **21**, no. 1, pp. 23–33, 2004.

Perrot, C., Panneton, R., and Olny, X., Periodic Unit Cell Reconstruction of Porous Media: Application to Open-Cell Aluminum Foams, *J. Appl. Phys*., vol. **101**, p. 113538, 2007.

Richardson, J. T., Peng, Y., and Remue, D., Properties of Ceramic Foam Catalyst Supports: Pressure Drop, *Appl. Catal. A*, vol. **204**, no. 1, pp. 19–32, 2000.

Smorygo, O., Mikutski, V., Marukovich, A., Ilyushchanka, A., Sadykov, V., and Smirnova, A., An Inverted Spherical Model of an Open-Cell Foam Structure, *Acta Mater*., vol. **59**, pp. 2669–2678, 2011.

Stemmet, C. P., Van der Schaaf, J., Kuster, B. F. M., and Schouten, J. C., Solid Foam Packing for Multiphase Reactors: Modeling of Liquid Holdup and Mass Transfer, *Chem. Eng. Res. Des*., vol. **84**, no. 12, pp. 1134–1141, 2006.

Stemmet, C. P., Meeuwse, M., Van der Schaaf, J., Kuster, B. F. M., and Schouten, J. C., Gas–Liquid Mass Transfer and Axial Dispersion in Solid Foam Packings, *Chem. Eng. Sci*., vol. **62**, no. 18-20, pp. 5444–5450, 2007.

Tschentscher, R., Nijhuis, T. A., Van der Schaaf, J., Kuster, B. F. M., and Schouten, J. C., Gas–Liquid Mass Transfer in Rotating Solid Foam Reactors, *Chem. Eng. Sci*., vol. **65**, no. 1, pp. 472–479, 2010.

Wenmakers, P. W. A. M., Van der Schaaf, J., Kuster, B. F. M., and Schouten, J. C., Enhanced Liquid–Solid Mass Transfer by Carbon Nano-Fibers on Solid Foam as Catalyst Support, *Chem. Eng. Sci*., vol. **65**, no. 1, pp. 247–254, 2010.

APPENDIX A.

For a square strut shape, $R_{\text{eq}} = A_s/\sqrt{\pi}$.

On substitution, we get

$$\varepsilon = 1 - \frac{\frac{1}{3}\left(36A_s^2 + 24.\frac{4}{3}A_s^3/\sqrt{\pi}\right)}{8\sqrt{2}L^3}$$

$$\Rightarrow 12\alpha_s^2\beta + \frac{32}{3\sqrt{\pi}}\alpha_s^3 = 8\sqrt{2}\,(1-\varepsilon) \qquad \text{(A.1)}$$

where $\alpha_s = A_s/L$ and $\beta = L_s/L$.

For a rotated square strut shape, $R_{\text{eq}} = A_{\text{rs}}/\sqrt{\pi}$.

On substitution, we get

$$\varepsilon = 1 - \frac{\frac{1}{3}\left(36A_{\text{rs}}^2 L_s + 24.\frac{4}{3}A_{\text{rs}}^3/\sqrt{\pi}\right)}{8\sqrt{2}L^3}$$

$$\Rightarrow 12\alpha_{\text{rs}}^2\beta + \frac{32}{3\sqrt{\pi}}\alpha_{\text{rs}}^3 = 8\sqrt{2}\,(1-\varepsilon) \qquad \text{(A.2)}$$

where, $\alpha_{\text{rs}} = A_{\text{rs}}/L$ and $\beta = L_s/L$.

For a diamond strut shape, $R_{\text{eq}} = A_{\text{det}}\sqrt{\sqrt{3}/2\pi}$.

On substitution, we get

$$\varepsilon = 1 - \frac{\frac{1}{3}\left(36\frac{\sqrt{3}}{2}A_{\text{det}}^2 L_s + 24.\frac{4}{3}.\frac{\sqrt{3}}{2}.\sqrt{\frac{\sqrt{3}}{2\pi}}A_{\text{det}}^3\right)}{8\sqrt{2}L^3}$$

$$\Rightarrow 6\sqrt{3}\alpha_{\text{det}}^2\beta + \frac{16}{\sqrt{3}}\sqrt{\frac{\sqrt{3}}{2\pi}}\alpha_{\text{det}}^3 = 8\sqrt{2}\,(1-\varepsilon) \qquad \text{(A.3)}$$

where $\alpha_{\text{det}} = A_{\text{det}}/L$ and $\beta = L_s/L$.

For a hexagon strut shape, $R_{\text{eq}} = A_h.\sqrt{3\sqrt{3}/2\pi}$.

On substitution, we get

$$\varepsilon = 1 - \frac{\frac{1}{3}\left(36\frac{3\sqrt{3}}{2}A_h^2 L_s + 24.\frac{4}{3}.\frac{3\sqrt{3}}{2}.\sqrt{\frac{3\sqrt{3}}{2\pi}}A_h^3\right)}{8\sqrt{2}L^3}$$

$$\Rightarrow 18\sqrt{3}\alpha_h^2\beta + 16\sqrt{3}\sqrt{\frac{3\sqrt{3}}{2\pi}}\alpha_h^3 = 8\sqrt{2}\,(1-\varepsilon) \quad \text{(A.4)}$$

where $\alpha_h = A_h/L$ and $\beta = L_s/L$.

For a rotated hexagon strut shape, $R_{\text{eq}} = A_{\text{rh}}.\sqrt{3\sqrt{3}/2\pi}$.

On substitution, we get

$$\varepsilon = 1 - \frac{\frac{1}{3}\left(36\frac{3\sqrt{3}}{2}A_{\text{rh}}^2 L_s + 24.\frac{4}{3}.\frac{3\sqrt{3}}{2}.\sqrt{\frac{3\sqrt{3}}{2\pi}}A_{\text{rh}}^3\right)}{8\sqrt{2}L^3}$$

$$\Rightarrow 18\sqrt{3}\alpha_{\text{rh}}^2\beta + 4\sqrt{3}\sqrt{\frac{3\sqrt{3}}{2\pi}}\alpha_{\text{rh}}^3 = 8\sqrt{2}\,(1-\varepsilon) \quad \text{(A.5)}$$

where $\alpha_{\text{h}} = A_{\text{rh}}/L$ and $\beta = L_s/L$.

For a star (regular hexagram) strut shape, $R_{\text{eq}} = A_{\text{st}}.\sqrt{3\sqrt{3}/\pi}$.

On substitution, we get

$$\varepsilon = 1 - \frac{\frac{1}{3}\left(36\sqrt{3}A_{\text{st}}^2 L_s + 24.\frac{4}{3}.3\sqrt{3}.\sqrt{\frac{3\sqrt{3}}{\pi}}A_{\text{st}}^3\right)}{8\sqrt{2}L^3}$$

$$\Rightarrow 36\sqrt{3}\alpha_{\text{st}}^2\beta + 32\sqrt{3}\sqrt{\frac{3\sqrt{3}}{\pi}}\alpha_{\text{st}}^3 = 8\sqrt{2}\,(1-\varepsilon) \quad \text{(A.6)}$$

where $\alpha_{\text{st}} = A_{\text{st}}/L$ and $\beta = L_s/L$.

APPENDIX B. APPENDIX B

Specific surface area of a square strut shape is given as

$$a_c = \frac{\left\{96A_sL_s + 24.\frac{3}{4}\left(\frac{5}{4}A_s^2\right)\right\}}{2\left(8\sqrt{2}L^3\right)} = \frac{1}{\sqrt{2}L}\left(6\alpha_s\beta + \frac{45}{32}\alpha_s^2\right) \quad \text{(B.1)}$$

Specific surface area of a rotated square strut shape is given as

$$a_c = \frac{\left\{96A_{\text{rs}}L_s + 24.\frac{3}{4}\left(\frac{5}{4}A_{\text{rs}}^2\right)\right\}}{2\left(8\sqrt{2}L^3\right)} = \frac{1}{\sqrt{2}L}\left(6\alpha_{\text{rs}}\beta + \frac{45}{32}\alpha_{\text{rs}}^2\right) \quad \text{(B.2)}$$

Specific surface area of a diamond strut shape is given as

$$a_c = \frac{\left\{96A_{\text{det}}L_s + 24.\frac{3}{4}\left[\frac{5}{4}\left(\frac{\sqrt{3}}{2}A_{\text{det}}^2\right)\right]\right\}}{2\left(8\sqrt{2}L^3\right)} = \frac{1}{\sqrt{2}L}\left(6\alpha_{\text{det}}\beta + \frac{45\sqrt{3}}{64}\alpha_{\text{det}}^2\right) \quad \text{(B.3)}$$

Specific surface area of a hexagon strut shape is given as

$$a_c = \frac{\left\{144A_hL_s + 24.\frac{3}{4}\left[\frac{5}{4}\left(\frac{3\sqrt{3}}{2}A_h^2\right)\right]\right\}}{2\left(8\sqrt{2}L^3\right)} = \frac{1}{\sqrt{2}L}\left(9\alpha_h\beta + \frac{135\sqrt{3}}{64}\alpha_h^2\right) \quad \text{(B.4)}$$

Specific surface area of a rotated hexagon strut shape is given as

$$a_c = \frac{\left\{144A_{\text{rh}}L_s + 24.\frac{3}{4}\left[\frac{5}{4}\left(\frac{3\sqrt{3}}{2}A_{\text{rh}}^2\right)\right]\right\}}{2\left(8\sqrt{2}L^3\right)} = \frac{1}{\sqrt{2}L}\left(9\alpha_{\text{rh}}\beta + \frac{135\sqrt{3}}{64}\alpha_{\text{rh}}^2\right) \quad \text{(B.5)}$$

Specific surface area of a star strut shape is given as

$$a_c = \frac{\left\{288A_{\text{st}}L_s + 24.\frac{3}{4}\left(\frac{5}{4}\left(3\sqrt{3}A_{\text{st}}^2\right)\right)\right\}}{2\left(8\sqrt{2}L^3\right)} = \frac{1}{\sqrt{2}L}\left(18\alpha_{\text{st}}\beta + \frac{135\sqrt{3}}{32}\alpha_{\text{st}}^2\right) \quad \text{(B.6)}$$